crystals

MDPI

Article

Microstructural, Mechanical and Wear Properties of Al–1.3%Si Alloy as Compared to Hypo/Hyper–Eutectic Compositions in Al–Si Alloy System

Ahmad Mostafa * and Nabeel Alshabatat

Department of Mechanical Engineering, Tafila Technical University, Tafila 66110, Jordan; nabeel@ttu.edu.jo
* Correspondence: a.omar@ttu.edu.jo; Tel.: +962-3225-0326

Abstract: The microstructure, mechanical properties, and wear behavior of three Al–Si alloys, namely: Al–1.3%Si, Al–1.5%Si and Al–13.5%Si were investigated. The specimens were examined by using an optical microscope to investigate the microstructural features of pin materials. Microhardness numbers and mechanical behavior parameters were determined by using a microhardness indenter and compression test, respectively. The dry sliding wear test was carried out using a pin-on-disc apparatus by varying the rotational speed (250, 350, and 450 rpm), normal load (5, 10 and 20 N) and test time (5, 10 and 15 min) at a constant sliding diameter of 300 mm. The surface roughness index (*Ra*) of the worn surfaces was determined by using a profilometer. The microstructure of Al–1.3%Si alloy was described as a fine eutectic colonizing in the *FCC-Al* phase matrix. Coarse eutectic dendrites surrounding the primary *FCC-Al* grains were observed in Al–1.5%Si alloy. The microstructure of Al–13.5%Si alloy showed a uniform layered structure of *FCC-Al* + *Diamond Si* eutectic. The average microhardness number was directly proportional to the Si concentration. Al–13.5%Si alloy with a high microhardness number (47.16 HV) showed excellent resistance to wear and exhibited a smoother surface at the end-of-wear test. The improved wear resistance in this case could be due to the presence of *Diamond-Si* hard phase in large quantities compared with other compositions. On the other hand, Al–1.5%Si alloy showed poorer resistance to wear because the mass loss action was dominated by a particle detachment mechanism. The response surfaces of the mass loss vs. speed, normal load and time showed increased mass loss when the three controlled parameters were increased. However, Pareto charts of the main effects of parametric interactions showed that the normal load was the main factor that must be considered when studying the tribological properties of Al–Si alloys.

Keywords: Al–Si alloys; mechanical behavior; microstructure; wear behavior; hypoeutectic composition; hypereutectic composition; DOE

Citation: Mostafa, A.; Alshabatat, N. Microstructural, Mechanical and Wear Properties of Al–1.3%Si Alloy as Compared to Hypo/Hyper–Eutectic Compositions in Al–Si Alloy System. *Crystals* **2022**, *12*, 719. https://doi.org/10.3390/cryst12050719

Academic Editors: Zhiwen Shao, Xiaoli Zhao, Chi Zhang and Bolv Xiao

Received: 18 April 2022
Accepted: 17 May 2022
Published: 18 May 2022

1. Introduction

Aluminum–silicon alloy components are commercially used in the automotive and aerospace industries as piston and bearing materials due to their low density, low thermal expansion coefficient, low cost, improved ambient temperature strength and good resistance to corrosion [1–5]. These components are subjected to severe mass loss during service. Thus, improving the tribological properties of Al–Si cast alloys becomes essential. Morphological differences between the microstructural constituents may significantly affect the tribological properties of cast Al–Si alloys [6]. For instance, the hard phases in Al–Si cast alloys solidify from a eutectic reaction that is mainly composed of hard and brittle *Diamond Si* plates and an *FCC-Al* solid solution matrix [7]. Commercial alloys may contain concentrations of silicon from hypoeutectic to hypereutectic with up to 30 wt.% Si [8]. In the case of a wide composition range, microstructure plays a significant role in determining the end properties of engineering materials. Understanding microstructure can determine the ultimate choice of a certain material's properties to be utilized in a proper application [9]. The tribological properties could be further influenced by the operating conditions,

such as sliding distance, sliding speed, load and temperature [6,10]. Yasmin et al. [11] investigated the tribological properties of cast Al–12.2% Si alloy by using a pin-on-disc dry sliding apparatus. The wear test parameters were rotational speed = 200, 300, and 400 rpm; load = 1.25, 2.50, and 3.75 kg; and sliding distance = 100, 1150 and 1550 m. According to these authors [11], the wear rate increased by increasing the rotational speed, load and sliding distance. However, increasing the input weight and sliding distance increased the mass loss intensively due to the frictional heat effect. Dwivedi [12] investigated the wear behavior of binary hypereutectic cast alloy Al–17%Si, by using a dry sliding wear test at 0.2–4.0 m/s sliding speeds and 10–30 N normal loads. They found that the wear rate decreased with an increase in sliding speed to a critical speed of approximately 3.0 m/s, after which it increased. The friction coefficient also decreased with the increase in sliding speed. Furthermore, the pin/disc interface temperature increased with the increase in sliding speed above 2.0 m/s. Kori and Chandrashekharaiah [13] investigated the dry sliding wear behavior of Al–Si alloys with a wide hypoeutectic composition range (0.2, 2, 3, 4, 5, and 7% Si) and compared the results with that of a eutectic composition containing 12% Si. In their experiments, the specific wear rate decreased with the increase in sliding speed and normal pressure with the incremental increase in Si content. Delaminative, adhesive, and abrasive wear mechanisms dominated the wear behavior of the examined alloys. Recently, Alshmri et al. [14] reviewed the dry sliding wear of Al–Si alloys and tabulated the wear rates ($m^3m^{-1} \times 10^{-12}$) of hypereutectic Al–Si alloys in the 12–25 wt.% Si composition range. No mutual comparison could be performed within the given data sets, because of the variant testing conditions used in experiments. It is important to mention that the results of dry sliding wear experiments, performed by Alshmri et al. [14], were not for binary Al–Si alloys to be compared with the results of this work. They provided results for multicomponent alloys containing Al, Si, Cu, Mg and Zr.

Because of their important tribological properties, the mechanical properties and wear resistance of Al–Si alloys of different compositions are studied. This work aims at examining the microstructure of three designed alloy compositions, Al–*x*%Si (x = 1.3, 1.5, and 13.5 wt.%), that fall in the *FCC-Al* solid solution, hypoeutectic and hypereutectic regions of the Al–Si binary alloy system, respectively. This is in contrast to the previous works which investigated the wear behavior of Al–Si alloys in the hypereutectic region only [11,12,14], and the work of [13] which focused mainly on the hypoeutectic region of Al–Si phase diagram. The mechanical behavior parameters (strength coefficients and strain hardening exponents) and microhardness numbers of the alloys were also determined in this work as important factors, in order to understand their impact on the tribological properties of investigated alloys which were not reported in previous studies. The wear behavior of Al–Si alloys was investigated by using a dry sliding wear test. The wear test was carried out using a pin-on-disc apparatus at different rotational speeds of 250, 350 and 450 rpm; several normal loads of 5, 10, and 20 N; and cumulative time intervals of 5, 10, and 15 min. The surface roughness index (*Ra*) for each designed alloy was defined at three orientations, 0°, 45°, and 90°, with respect to the wear track direction. The previous studies [11–14], covered in this work, provided the wear behavior of Al–Si alloys based on the influence of a one-at-a-time wear test parameter only. Furthermore, no statistical approaches were used to determine the most influential parameter on the wear behavior of the investigated alloys. However, in this work, response surfaces were plotted using the full factorial design of experiments (DOE) method to describe the effect of wear test parameters on the performance of the tested specimens. The effect of the most influential parameter and/or interaction of parameters on the wear behavior of the alloys was described using Pareto Chars.

2. Experimental Procedure

The starting materials for the investigated alloys were Al ingots with 99.7% purity, supplied by Alfa Aesar, a Johnson Matthey Company, and Si pieces with 99.95%, supplied by Sigma Aldrich (Missouri, United States). It is important to mention that the effect of trace

elements in all experiments was neglected because of their extremely low concentrations. Three Al–Si binary alloys with 1.3, 1.5, and 13.5 wt.% Si were prepared by melting the predetermined quantities of Al and Si metals in a graphite crucible by using an electric arc furnace. The chemical compositions of the prepared specimens are listed in Table 1.

Table 1. Chemical compositions (wt.%) of the three tested specimens in this work.

Specimen	Al (wt.%)	Si (wt.%)
FCC-Al solid solution	98.7	1.3
Hypoeutectic	98.5	1.5
Hypereutectic	86.5	13.5

The metals were alloyed at 740 °C and calcium fluoride (CaF_2) was added to prevent alloy oxidation. The melt was stirred by using a graphite rod and the furnace temperature was raised to approximately 800 °C for 15 min to enhance the homogeneity of the alloys. Then, the melts were poured in preheated cylindrical copper dies to solidify under slow cooling conditions. Slow cooling rates were adopted to eliminate the formation of the non-uniform as-cast microstructures that typically appear due to high cooling rates. The alloys were prepared according to the terminal solid solubility limit of Si in Al and to the eutectic composition in the Al–Si phase diagram [15]. The partial Al–Si phase diagram shown in Figure 1, was calculated using an FTlite database, developed by Scientific Group Thermodata Europe (SGTE) [16] in Factsage® thermochemical software [17] to show the compositions of the investigated alloys.

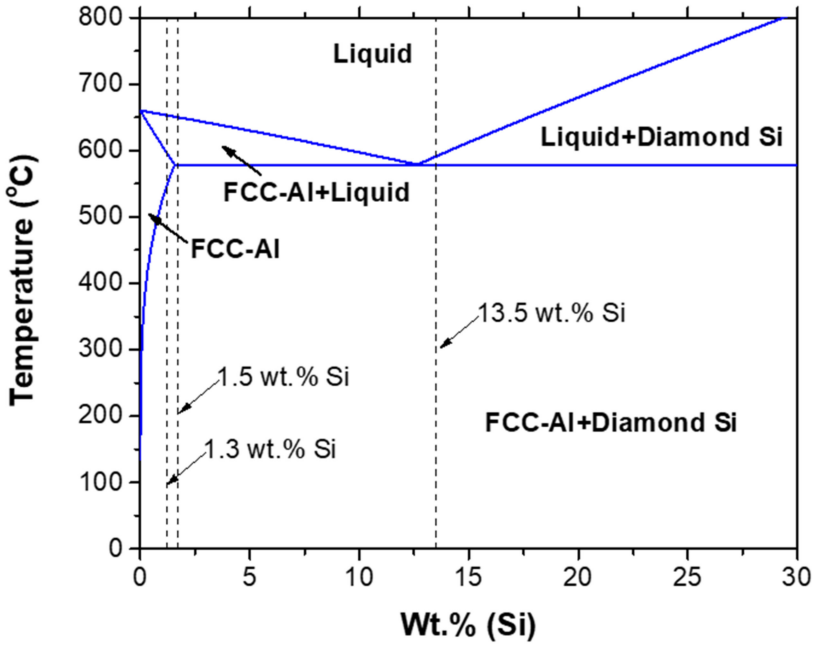

Figure 1. The calculated Al–Si partial phase diagram near the Al-rich terminal side.

The Al–1.3% Si alloy was designed to contain a lower eutectic composition and a higher *FCC-Al* phase content. The Al–1.5% Si alloy was designated as the hypoeutectic composition, and the Al–13.5% Si alloy was designated as the hypereutectic composition. The prepared alloys were sliced into several pieces using a slow cutting machine to minimize the heat generated during the cutting process and to prevent any microstructural changes. The specimens used for metallographic inspection were mounted in cold epoxy blocks, ground gradually from 240 up to 1200 grit by using SiC sandpapers, and polished by using 1 μm diamond suspension. The polished specimens were chemically etched by

using Tucker's reagent (15 mL HF + 15 mL HNO_3 + 45 mL HCl + 25 mL distilled water) for 10–30 s of exposure to the solution. Microhardness tests were carried out on the polished surfaces by using a Highwood HWDM-3 Vickers hardness tester with 100 g load. Ten different values were taken at different locations from which the average HV number for each alloy was determined. The compression test was carried out on cylindrical specimens of 10 mm diameter × 10 mm length. The cylinders were compressed at room temperature by using a Quasar 100 universal testing machine of 100 KN capacity with 1×10^{-3} s^{-1} strain rate. The load–extension data were recorded by a data acquisition system to evaluate true stress–strain data from which the strength coefficient and strain hardening exponent could be calculated. The wear behavior of the three alloys was evaluated according to an ASTM G99 standard test [18], using a pin-on-disc wear test apparatus. The tested specimens were subjected to dry sliding against a carbon steel disc thermally coated with hard chromium particles of 65 HRC. The schematic of the pin-on-disc wear test apparatus is shown in Figure 2 [19].

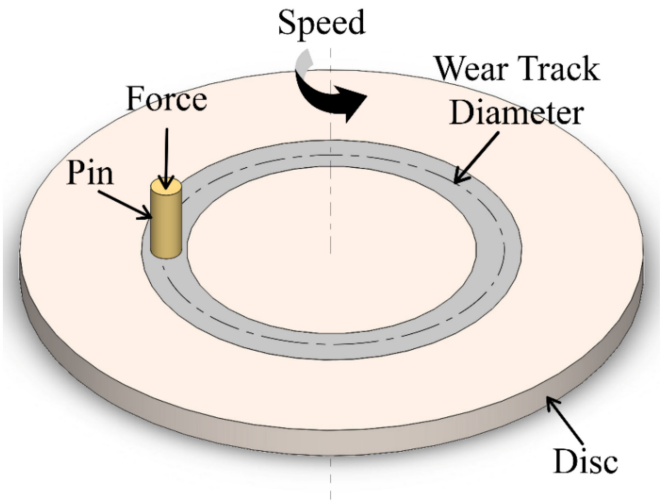

Figure 2. Illustration of pin-on-disc wear test apparatus setup and testing parameters.

The wear test was performed by using 250, 350, and 450 rpm speeds at a track radius of 50 mm and three different normal loads of 5, 10, and 20 N. The total test period for each experiment was 15 min where the pin was weighed after each 5 min time span by using a 0.1 mg balance. The cleaning process involved dipping the worn specimen in an alcohol bath associated with gentle stirring to self-drop debris from worn surfaces. The use of the ultrasonic cleaning method was not adopted in this work because it may result in removing some parts of the tribolayers when applied [20]. The experimental conditions used in the wear test experiments are listed in Table 2. For each individual test, the friction force was recorded from the test apparatus directly. The wear behavior of the test specimens was evaluated in terms of the mass loss.

Table 2. Wear test experimental conditions.

Factors	Values		
Sliding diameter (mm)		100	
Rotational speed (rpm)	250	350	450
Sliding speed (m/s)	1.31	1.83	2.36
Load (N)	5	10	20
Time (min)	5	10	15

The 2D surface roughness patterns were measured at 0°, 45°, and 90° orientations for all specimens tested under the most severe conditions used in the current work (450 rpm, 20 N load, and 15 min time). The average surface roughness (*Ra*) numbers were used to

evaluate the surface quality of the worn specimens. Surface roughness (*Ra*) measurements were acquired by using a Surfcoder SE600 surface roughness measuring instrument according to ISO 13565 (Rk) standards. A transverse length of 4 mm, cut-off length of 0.8 mm and pitch of 0.0005 mm were used to plot the surface height (µm) versus sampling length (mm) for all specimens. A full factorial design of experiments (DOE) in the form of 2^k experiments was employed to identify the effect of the parametric interactions of the wear test conditions on the amount of mass loss, and to determine the most dominant factor. Number 2 represents the number of levels used in the wear experiments (high and low levels) and the factor *k* refers to the number of variables (load, speed and time). The sliding radius was kept constant at 300 mm for all experiments. The 3D response surfaces were plotted accordingly to evaluate the optimal performance of the alloys under dry sliding wear conditions.

3. Results and Discussion

3.1. Microstructure Analysis

The optical micrographs of the three investigated alloys, namely, Al–1.3%Si, Al–1.5%Si and Al–13.5%Si, at room temperature are illustrated in Figure 3. High magnification images (right column) are provided to highlight the microstructural features in all compositions. The microstructural findings can be explained properly by understanding the Al–Si binary phase diagram.

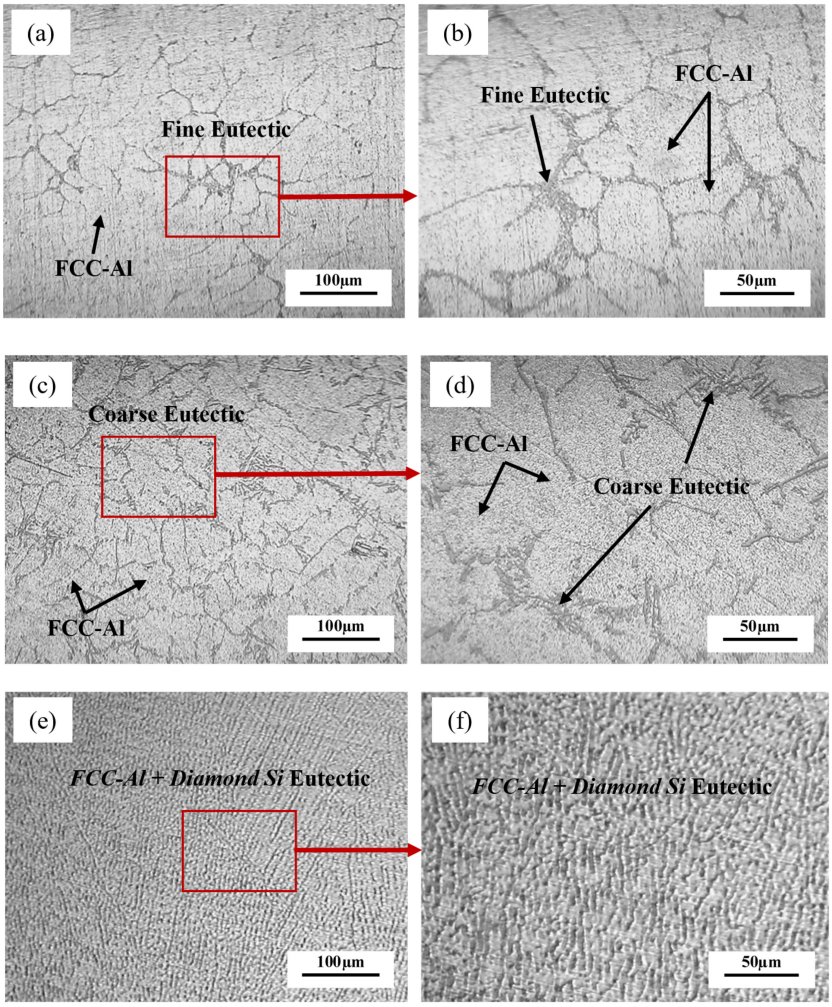

Figure 3. Optical micrographs of (**a**,**b**) Al–1.3%Si alloy, (**c**,**d**) Al–1.5%Si alloy, and (**e**,**f**) Al–13.5%Si alloy at different magnifications to highlight the microstructural features.

Several studies have been carried out to describe the phase relations in the Al–Si binary system. Mostafa and Medraj [15] critically reviewed the available experimental and thermodynamic data in the literature and provided an acceptable version of the system. According to the updated Al–Si system [15], the eutectic reaction *Liquid* ⇄ *FCC-Al* + *Diamond Si* occurs at 11.78 wt.% Si and 577 °C. The terminal solid solubility of Al-rich side is approximately 1.44 wt.% Si at the eutectic temperature and the solubility of Al in Si-rich side is considered negligible. Figure 3a,b exhibit the microstructure of Al–1.3% Si alloy. This alloy was designed to give insights into the microstructure of the terminal solid solution in the Al-rich side. At room temperature, the alloy falls in the *FCC-Al* + *Diamond Si* two-phase field, where the *FCC-Al* composition drops from 1.3 wt.% Si at 577 °C to less than 0.01 wt.% Si at room temperature. It is conventionally known that primary *FCC-Al* phase forms in the *Liquid* + *FCC-Al* two-phase field upon cooling the molten alloy down to approximately 650 °C, and the remaining liquid is supposed to transform into *FCC-Al* phase at 590 °C because the composition passes through the single-phase region. With further cooling to room temperature, the composition enters the *FCC-Al* + *Diamond Si* two-phase field at 550 °C and silicon becomes supersaturated in the *FCC-Al* solid solution. The excess silicon is repelled from the solid solution to form fine eutectic morphology. Therefore, the microstructure of Al–1.3 wt.% Si alloy shows large grains of primary (proeutectic) *FCC-Al* phase surrounded by a fine eutectic structure. The fine eutectic occurs due to the far shifting of the alloy composition from the eutectic point. The cooling path of Al–1.3% Si alloy can be depicted as follows:

$$Liquid \rightarrow Liquid + FCC\text{-}Al \rightarrow FCC\text{-}Al \rightarrow FCC\text{-}Al + Diamond\ Si$$

Figure 3c,d represent the room temperature microstructure of Al–1.5% Si hypoeutectic alloy. The microstructure exhibits smaller *FCC-Al* phase grains and coarser eutectic morphology than that shown by Al–1.3% Si due to a higher Si concentration in Al–1.5% Si alloy. The primary *FCC-Al* phase in the hypoeutectic alloy was precipitated from liquid in the *Liquid* + *FCC-Al* two-phase field at 650 °C upon cooling. The remaining liquid solidifies below 577 °C and forms the *FCC-Al* + *Diamond Si* eutectic structure. The cooling path of Al–1.5% Si alloy did not pass through the *FCC-Al* single-phase field. Instead, it followed the path depicted below:

$$Liquid \rightarrow Liquid + FCC\text{-}Al \rightarrow FCC\text{-}Al + Diamond\ Si$$

The microstructure in Figure 3e,f belongs to the hypereutectic alloy which contains 13.5 wt.% Si. The eutectic structure can be easily recognized in this alloy by the uniform layered *FCC-Al* + *Diamond Si* morphology. Only 0.87% of *Diamond Si* was precipitated in the *Liquid* + *Diamond Si* two-phase field prior to the eutectic line (at approximately 578 °C) due to the very low solubility of Al in liquid Si [15]. The eutectic transformation occurred below 577 °C and *FCC-Al* + *Diamond Si* eutectic formed down to room temperature. The cooling path of the hypereutectic alloy can be depicted as follows:

$$Liquid \rightarrow Liquid + Diamond\ Si \rightarrow FCC\text{-}Al + Diamond\ Si$$

It is important to mention that the primary (pro-eutectic) *Diamond Si* phase did not appear in the microstructure of the hypereutectic alloy because of the negligible solid solubility of Al in Si, and thus only a layered structure was observed without *Diamond Si* clusters.

3.2. Microhardness Analysis

The plots of microhardness numbers for all investigated alloys are given in Figure 4. It is important to mention that the microhardness device is calibrated using standard procedures on a regular basis prior to performing and testing. The average of 10 readings was plotted by using a dashed line across the data points in association with the average microhardness number printed inside each figure.

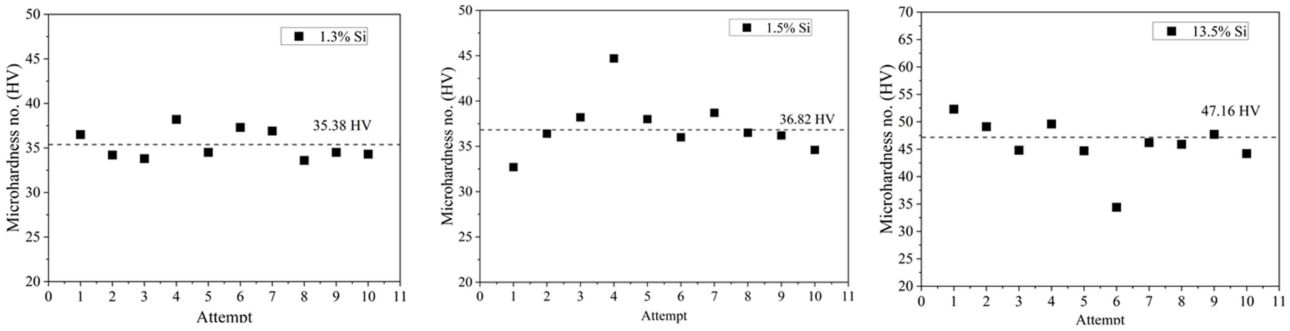

(**a**) (**b**) (**c**)

Figure 4. Microhardness values and average microhardness numbers for (**a**) Al–1.3%Si, (**b**) Al–1.5%Si, and (**c**) Al–13.5%Si alloys.

The average microhardness numbers recorded for Al–1.3% Si, Al–1.5% Si, and Al–13.5% Si alloys were 35.38, 36.82, and 47.16 HV, respectively. The obtained microhardness values in this work are in the same range of that reported by Gupta and Ling [21]. It is clear that the average microhardness numbers are directly proportional to the Si concentration [22] in Al–Si alloy system. The 10 microhardness points in Figure 4a are less scattered than those presented in other figures as an indication of a good-calibrated instrument. The microhardness indenter was presumed to land mainly on the soft *FCC-Al* phase which is largely available in Al–1.3% Si alloy as can be depicted from the microstructure in Figure 3a. Figure 5a shows the trace of the microhardness indenter on the surface of Al–1.3% Si alloy which demonstrates the microstructure of the indenter region and the indenter features. More fluctuating values are observed in Figure 4b, which represents the microhardness profile across Al–1.5% Si alloy. In this alloy, the low microhardness numbers reflect the hardness of the soft *FCC-Al* phase because the values were consistent with those obtained from Figure 4a. However, the jump in the microhardness number (point 4) indicates the landing of the microhardness indenter on a hard phase that contains a higher Si concentration than that existing in the *FCC-Al* solid solution. The microstructure in Figure 3c shows that the formation of coarse eutectic morphology is at the expense of *FCC-Al* phase due to the increased Si concentration in Al–1.5% Si alloy compared with that in Al–1.3% Si alloy. With the increase in the area of coarse eutectic, the chances of gaining microhardness values from these regions increase and the average microhardness number also increases. Figure 5b illustrates the microstructure of the microhardness indenter region of Al–1.5 Si alloy. It can be noted that the indenter landed on a region with coarser eutectic dendrites, thereby explaining the increased microhardness number.

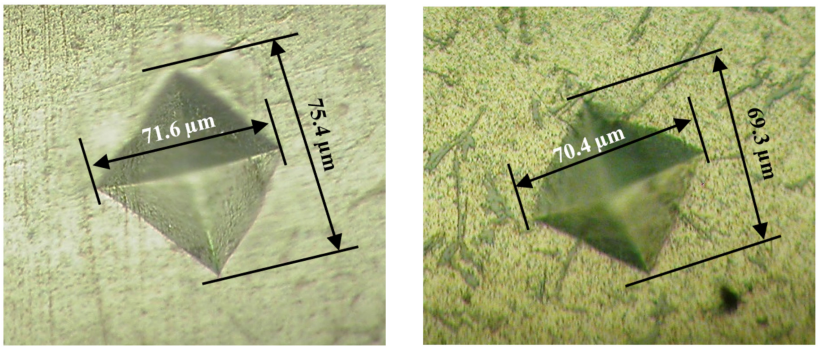

(**a**) (**b**)

Figure 5. Microhardness indenter traces on the surfaces of (**a**) Al–1.3% Si and (**b**) Al–1.5% Si alloys to illustrate the microstructural features underneath each indentation.

It is important to note that the higher microhardness number observed in Figure 4b at point 4 is consistent with the values obtained from Al–13.5% Si alloy in Figure 4c, which mainly contains *FCC-Al + Diamond Si* eutectic as exhibited in Figure 3e. The drop occurred in Figure 4c at point 6 could be due to impurity, or the indenter landing on a vacant location. The consistency in the microhardness values between Figure 4a,b and Figure 4b,c provides experimental support to the microstructural findings in Figure 3 in terms of constituents and phase quantities.

3.3. Compression Test Analysis

The mechanical behaviors of the investigated alloys are represented in Figure 6. The true stress–true strain curves shown in Figure 6a were calculated from the compression test results. The compression test was stopped at the same point for all specimens and thus the strain seems at the same level for all tests. Figure 6b shows the log stress–log strain curves plotted from the true stress–true strain values to calculate the strength coefficients (K) and strain hardening exponents (n) for all specimens in this study. Table 3 summarizes the mechanical behavior parameters for all examined alloys obtained from the compression test.

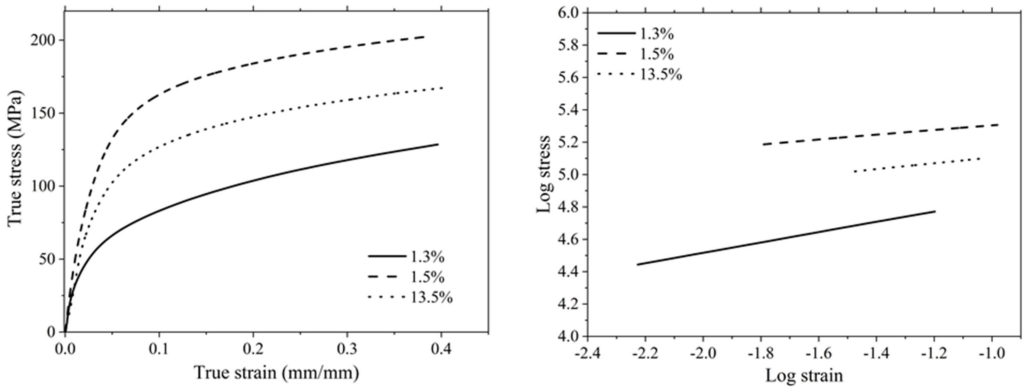

Figure 6. (**a**) True stress-strain and (**b**) log stress-log strain curves obtained from compression test for all examined alloys.

Table 3. Mechanical behavior parameters (strength coefficient and strain hardening exponent) of the examined alloys.

Alloy	0.2% Proof Stress (MPa)	Strength Coefficient (MPa)	Strain Hardening Exponent
Al–1.3%Si	47.66	173.3	0.3193
Al–1.5%Si	131.99	233.3	0.1475
Al–13.5%Si	109.02	197.3	0.1792

The flow curves in Figure 6a did not show a clear yield point, and thus the proof stress values were calculated in Table 3 at 0.2% strain. It is noted that the highest proof stress was recorded as 131.99 MPa for Al–1.5% Si which contains small *FCC-Al* grains and coarse eutectic morphology in its microstructure. The coarse eutectic was uniformly distributed within the pro-eutectic *FCC-Al* matrix unlike the fine eutectic that colonized in the Al–1.3% Si alloy. The coarse eutectic surrounded the *FCC-Al* grains and played an important role in blocking the dislocation motion upon stressing the material. Moreover, the small *FCC-Al* grain size increased the grain boundary areas which enhanced the strength properties of the hypoeutectic alloy [23]. Thus, the proof stress increased significantly. However, the lowest proof stress value was recorded as 47.66 MPa for Al–1.3% Si. This finding could be due to the connected soft *FCC-Al* grains within the fine eutectic colonies, as concluded

from the microstructure in Figure 3a. In this case, the mechanical behavior of this alloy is mainly demonstrated by the soft phase. *FCC-Al* is termed as the soft phase in this work due to its low average microhardness number given in Figure 4a.

The Al–13.5% Si alloy showed a moderate proof stress value of 109.02 MPa. This composition exhibited a microstructure of uniform *FCC-Al* + *Diamond Si* eutectic layers. Both existing phases have dissimilar crystal structures and contrary morphological characteristics. It is assumed that the moderate proof stress value was due to the lattice mismatch between non-faceted *FCC-Al* and faceted (plate-like) *Diamond Si* morphologies [24]. Furthermore, the *Diamond Si* layers in the Al–Si alloy eutectic structure deteriorate the ductility and toughness of the material because they act as crack propagation paths [25]. The crystallographic data for the solid phases in Al–Si binary system are listed in Table 4 [15].

Table 4. Crystallographic data of the solid phases in the Al–Si binary systems.

Phase	Prototype	Lattice Parameter *a* (nm)	Space Group Number	Space Group
FCC-Al	Cu	0.4047	225	*Fm-3m*
Diamond Si	C (Diamond)	0.5430	227	*Fd-3m*

The calculated *K* and *n* values were compatible with the proof stress values reported in Table 3. This compatibility could be due to the same reasons that influenced the proof stress behavior, as discussed previously. It is important to mention that *K* and *n* were calculated in the plastic deformation region to fulfill the Hollomon equation, which is a power law relating the true-plastic stress to the true-plastic strain raised to the power *n* [26]. The high *n* value exhibited by Al–1.3% Si alloy can refer to the capability of *FCC-Al* grains to uniformly distribute the deformation. In other words, *n* is used to evaluate the strain hardening capability of the material [27]. Thus, it is concluded that Al–1.3% Si can be easily cold-worked compared with the hypoeutectic and hypereutectic samples. Moreover, the hypereutectic sample showed a better response to cold-working than the hypoeutectic sample.

3.4. Wear Behavior

A dry sliding wear test was performed to describe the wear behavior of the three Al–Si compositions suggested in this work under the operation conditions listed in Table 2. The wear test stages were carried out sequentially where the pin of each alloy composition was initially weighed and then tested in the following manner: 250 rpm @ 5 N, 10 N and 20 N → 350 rpm @ 5 N, 10 N and 20 N → 450 rpm @ 5 N, 10 N and 20 N. Thus, the initial weight of the pin at the beginning of each test equals the final weight of the pin in the previous stage. Figure 7 summarizes the wear behavior results of the examined alloys in terms of the cumulative mass loss (g) vs. test time (minute) under three normal loads (N) and at three rotational speeds (rpm). It is notable that the mass loss is directly correlated with time, normal load and rotational speed for all specimens. In other words, the mass of the pin decreases by increasing the test time, normal load and rotational speed. Figure 7a–c shows the cumulative mass loss vs. time and normal load plots for Al–0.13%Si alloy at 250, 350 and 450 rpm, respectively. The influence of rotational speed on the wear behavior of Al–1.3% Si alloy can be concluded by comparing the values on *y*-axis in the three Figure 7a–c). The total mass loss after performing the 250 rpm @ 20 N test stage was 0.019 g. On the other hand, the amount of lost mass increased up to 0.0302 g after performing the 350 rpm @ 20 N wear test and reached up to 0.0522 g after the 350 rpm @ 20 N wear tests. A similar trend was observed in the wear test results of other alloy compositions as demonstrated in Figure 7d–i under the given experimental conditions.

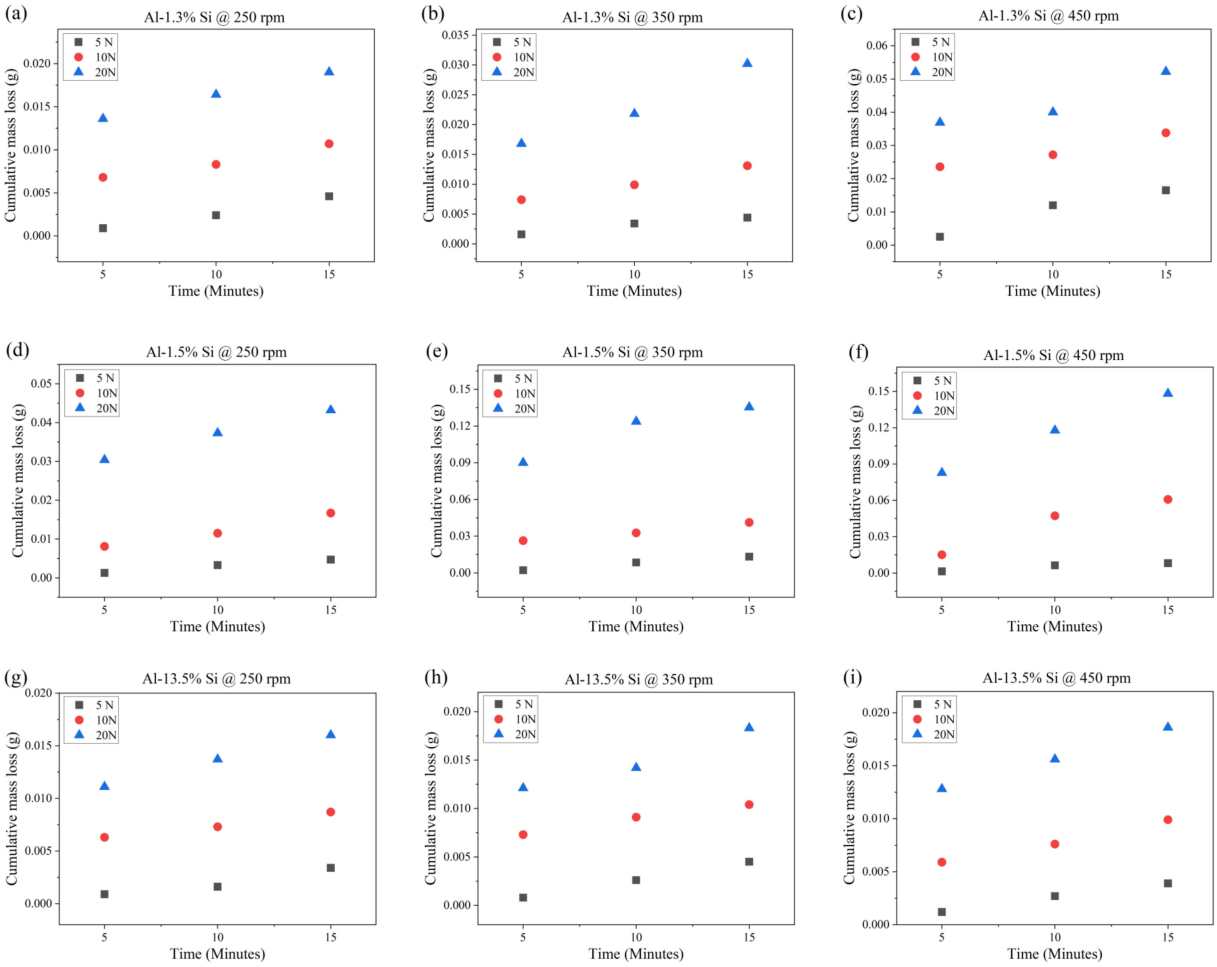

Figure 7. Cumulative mass loss vs. time plots as functions of normal load (5, 10, and 20 N) and rotational speed (250, 350, and 450 rpm) for (**a**–**c**) Al–1.3%Si; (**d**–**f**) Al–1.5%Si; and (**g**–**i**) Al–13.5%Si alloys.

The reason for the increased mass loss as a function of rotational speed could be due to the combined changes arising from the heat of friction and strain rate that is expected with increased sliding speed [28,29]. The friction temperature was acquired during the wear test and plotted vs. time as a function of normal load and rotational speed as shown in Figure 8. The plots indicate that the temperature of the specimens increases with the increase in rotational speed and normal load. Ozioko [29] reported that the increased temperature with rotational speed can be due to the increased sliding distance in the wear test for each time interval, which generates more heat at the pin–disc interface. Moreover, Yasmin et al. [11] indicated that the increased friction temperature may soften the pin material, making it easier to damage. The increase in mass loss with an increasing normal load is attributed to the consequential strain hardening of the test specimen that leads to more plastic deformation [11,29]. Additionally, the increased normal load enhances the contact area between the mating parts and thus the friction at the pin–disc interface increases [11]. The high frictional force indicates the generation of a high frictional temperature.

Figure 9 is plotted to emphasize the influence of alloy composition on the wear behavior of Al–Si alloys. The data points represent the cumulative mass loss of the pin after the 15 min test period. The most significant mass loss (higher wear rate) was related to the Al–1.5%Si alloy, equating to 0.0432, 0.1354, and 0.1481 g at 250, 350, and 450 rpm, respectively. Whereas the least mass loss (lowest wear rate) was observed in Al–13.5%Si alloy which is 0.016, 0.0183, and 0.0186 g at 250, 350, and 450 rpm, respectively. It is noted that the mass loss decreased (lower wear rate) when the composition of silicon was increased. A similar conclusion was reached by Ozioko [29] who examined Al–Si alloys

in the 7–14%Si composition range. However, the sample with the lower Si concentration, Al–1.3%Si, exhibited an intermediate mass loss of approximately 0.019, 0.0302, and 0.0522 g at 250, 350, and 450 rpm, respectively.

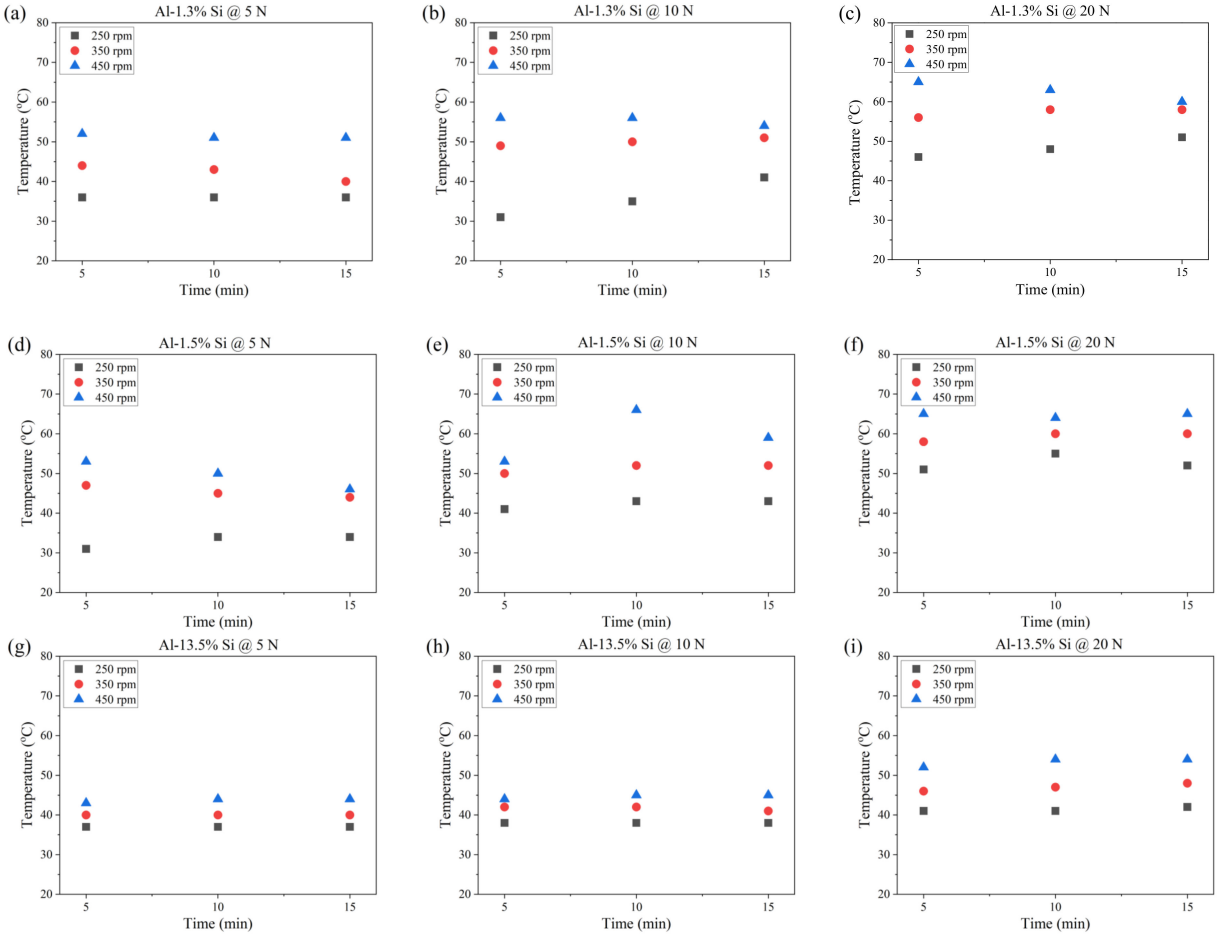

Figure 8. Friction temperature vs. time plots as functions of normal load (5, 10, and 20 N) and rotational speed (250, 350, and 450 rpm) for (**a**–**c**) Al–1.3%Si; (**d**–**f**) Al–1.5%Si; and (**g**–**i**) Al–13.5%Si alloys.

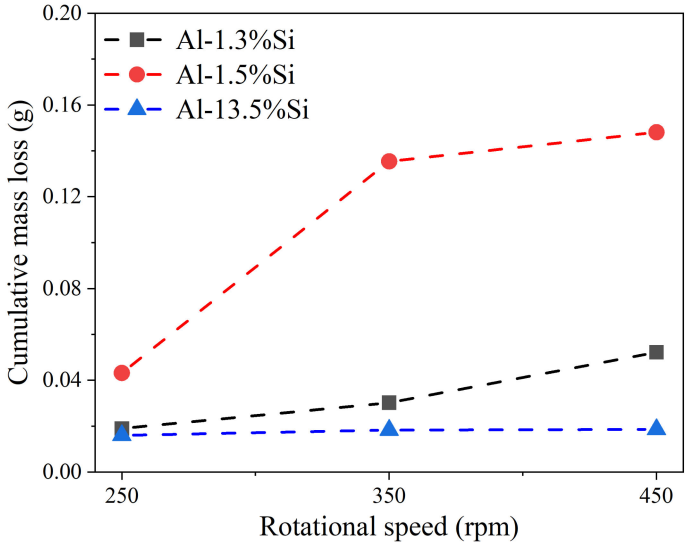

Figure 9. Cumulative mass loss vs. rotational speed plot as a function of alloy composition.

The increased wear resistance of Al–13.5%Si alloy can be related to the high Si concentration which modifies the microstructure and increases the microhardness number, as discussed in the previous sections. The Al–Si eutectic composes of *FCC-Al* + *Diamond Si* solid solutions as shown in Figure 3e. The amount of *FCC-Al* in the eutectic reaches the maximum at the eutectic point and then decays with the further increase in Si concentration. *FCC-Al* is considered the softer phase in the eutectic as concluded from the microhardness analyses in Section 3.2. Thus, the highest amount of hard phase (*Diamond Si*) exists in Al–13.5%Si alloy among other examined specimens. The wear rate is reversibly proportional to the microhardness number [23] and this conclusion is consistent with the reported results in this work because Al–13.5%Si alloy has the lowest mass loss and a higher microhardness number.

Both Al–1.3%Si and Al–1.5%Si alloys have a low Si concentration and close average microhardness numbers. However, Al–1.3%Si alloy showed enhanced wear behavior compared with Al–1.5%Si alloy. The enhanced wear behavior could be due to the presence of soft phase (*FCC-Al* solid solution) in high percentages. The asperities of soft materials usually tend to plastically deform rather than break under the actions of normal and shear forces developed during the wear test [10,30]. The plastic deformation was found to increase the frictional forces and thus increase the sample temperature. This phenomenon was observed in Figure 8a–f, where the acquired temperatures for Al–1.3%Si and Al–1.5%Si alloys were higher than that for Al–13.5%Si alloy due to the high percentage of soft phase in the two compositions. The microstructure of Al–1.5%Si alloy is dominated by *FCC-Al* + *Diamond Si* coarse eutectic distributed uniformly in the primary *FCC-Al* phase. Thus, the microstructure of this alloy is neither dominated by a soft phase nor a hard phase, compared with the Al–1.3%Si and Al–13.5%Si alloys, respectively. The coarse eutectic dendrites appear to surround the *FCC-Al* grains (Figure 3c), isolating the large *FCC-Al* grains through the phase boundaries. The wear mechanism in this alloy may result from the *FCC-Al* grain detachment from the surface of the pin [4]. On the other hand, smaller *Diamond Si* particles may detach from *FCC-Al* matrix during sliding and remain on the disc surface. The mass loss due to remaining particles could be dominated by abrasive wear mechanism [31]. In fact, this explains the reasons for the significant loss of Al–1.5%Si alloy mass during the dry sliding wear test.

3.5. Surface Roughness

The surface roughness profiles of the tested specimens were examined at the most severe testing conditions, that is, 450 rpm rotation speed, 15 min testing period and 20 N normal load, and at three different orientations with respect to the direction of the surface streaks, that is, 0°, 45°, and 90°, as shown in Figure 10a–c. Accordingly, the roughness index (*Ra*) values were calculated from each roughness profile and presented in Figure 10d. The results indicated that the Al–13.5% Si alloy has the lowest surface roughness values of *Ra* = 0.76, 2.93 and 3.19 at 0°, 45°, and 90° directions, respectively. Whereas the roughness profile of Al–1.5% Si specimen showed the highest surface roughness values among other tested compositions with *Ra* = 2.21, 6.17 and 7.83 at 0°, 45° and 90° directions, respectively. With reference to Figure 4, a reverse relationship between the roughness and microhardness values could be depicted, where the roughness value decreases with increased microhardness number. As discussed in Section 3.5, the presence of *Diamond Si* hard phase in the Al–Si eutectic reduced the mass loss (enhanced the wear behavior) of Al–13.5% Si alloy and thus it is expected to give the lowest *Ra* value. On the other hand, the abrasive wear mechanism that occurred in Al–1.5%Si alloy may leave deep crates on the surface of the tested pin, which is expected to increase the *Ra* value [31].

3.6. Design of Experiments and Response Surfaces

The impact of changing one factor at a time might be inadequate to demonstrate the wear behavior of examined alloys under the influence of several factors. Thus, a full factorial design of experiments was adopted to describe the wear behavior under the

influence of several parameter interactions. Three factors (speed, load and time) were used in this study and thus, $k = 3$. Each factor was tested under two experimental levels (low and high) as follows: 250 and 450 rpm for the speed, 5 and 20 N for the normal load, and 5 and 15 min for the time intervals. Thus, the factorial design for this experiment is (2^3) and the number of interactions was eight for each alloy composition as listed in Table 5.

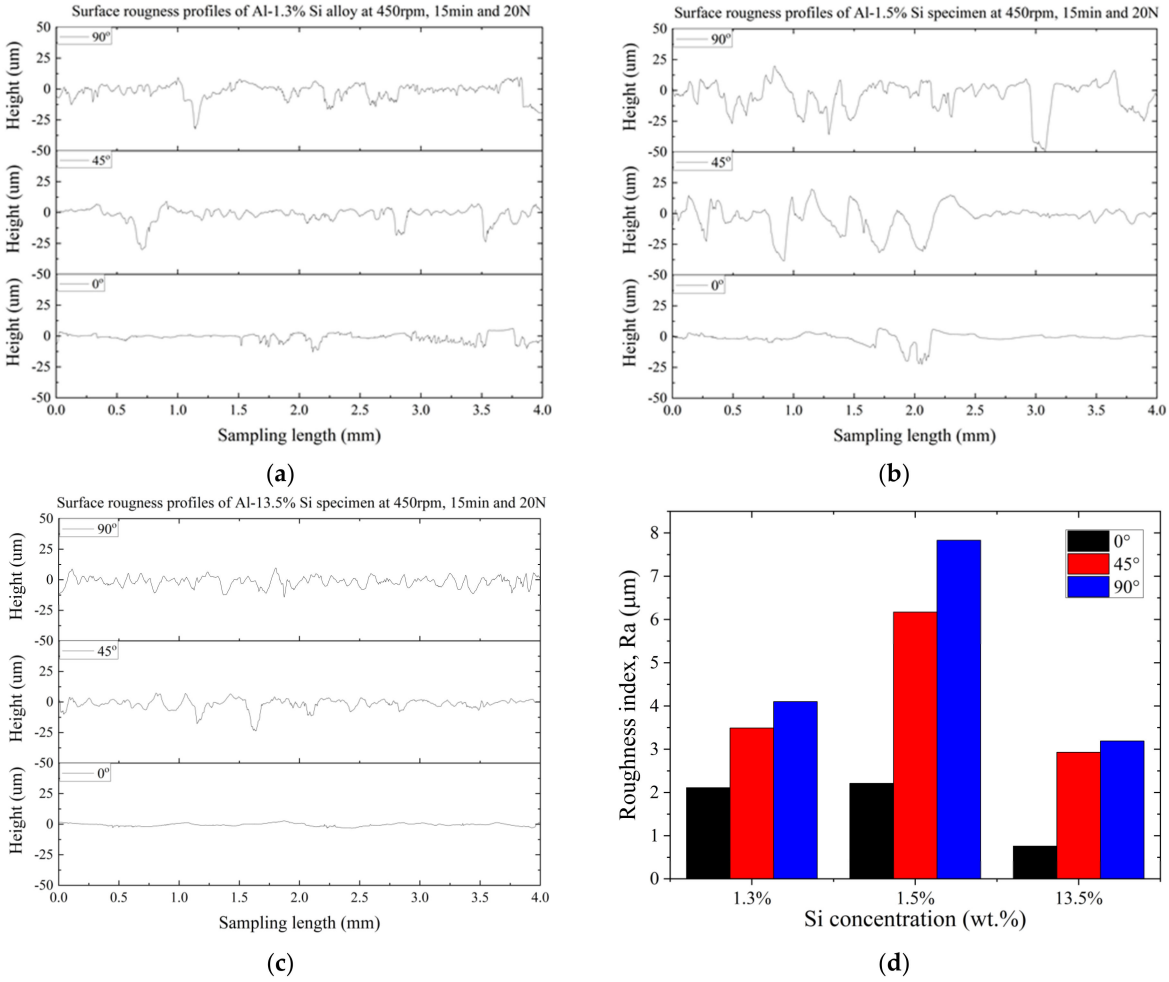

Figure 10. (**a**–**c**) Surface roughness profiles for Al–1.3%Si, Al–1.5%Si, and Al–13.5%Si alloys, respectively, in three directions, i.e., 0°, 45°, and 90° to the streak direction. (**d**) Roughness indices at 0°, 45°, and 90° versus Si concentration for the three Al–Si compositions.

Table 5. List of test conditions for each alloy composition.

Iteration	Level of Each Factor			Cumulative Mass Loss Responses		
	Speed	Normal Load	Time	Al–1.5% Si	Al–1.3% Si	Al–13.5% Si
1	−1	1	−1	0.0136	0.0304	0.0111
2	1	−1	1	0.0165	0.0082	0.0039
3	−1	−1	1	0.0046	0.0047	0.0034
4	1	−1	−1	0.0025	0.0014	0.0012
5	1	1	1	0.0522	0.1481	0.0186
6	−1	1	1	0.0190	0.0432	0.0160
7	1	1	−1	0.0369	0.0827	0.0128
8	−1	−1	−1	0.0009	0.0013	0.0009

The response surfaces of cumulative mass loss vs. speed, normal load and time for Al–1.3%Si, Al–1.5%Si and Al–13.5%Si alloys are illustrated in Figure 11a–i, respectively. In all figures, the cumulative mass loss showed an increased trend when the three factors (speed, normal load and time) were in the high level. Under such conditions, it is not easy to determine the effect of each individual factor.

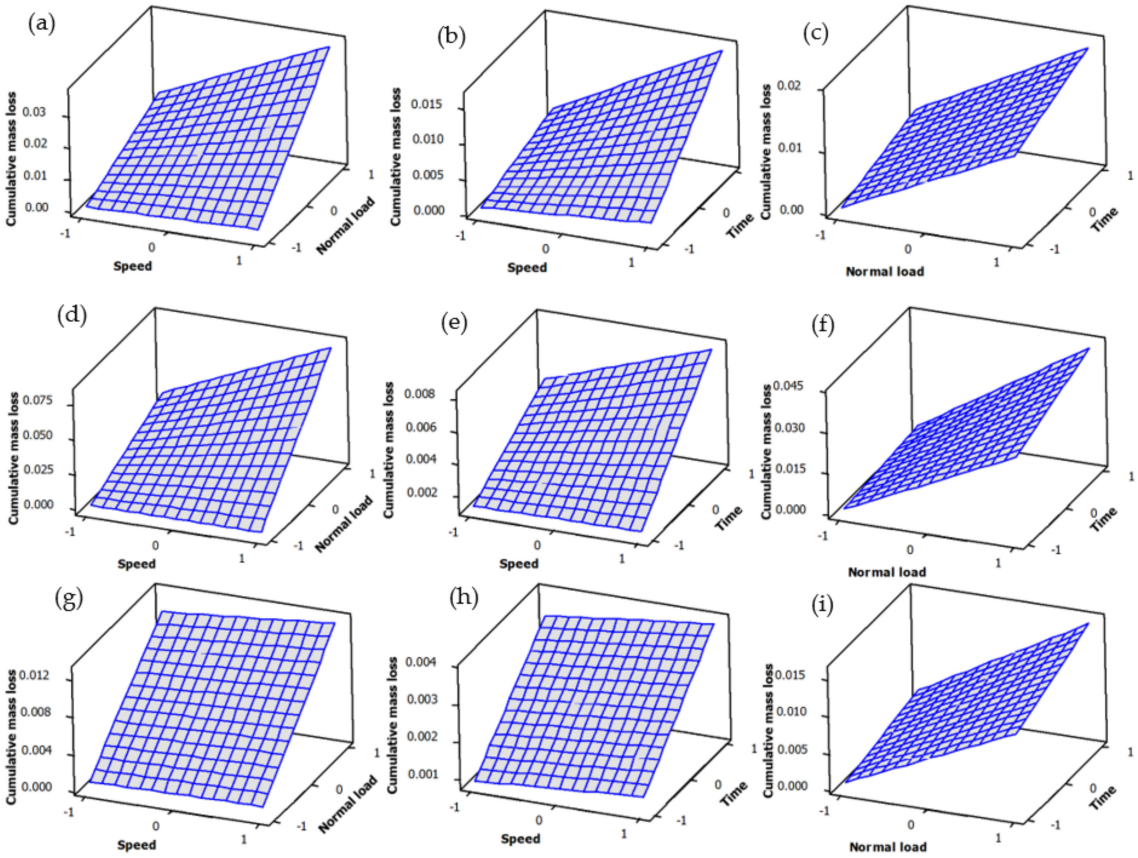

Figure 11. Response surfaces of cumulative mass loss vs. normal load and speed, time and speed, and time and normal load for (**a**–**c**) Al–1.3%Si, (**d**–**f**) Al–1.5%Si and (**g**–**i**) Al–13.5%Si alloys.

To explore the effect of individual factors and their interactions, Pareto charts of the main parametric effects are plotted in Figure 12. The reliability of the estimated effects from these charts can be estimated by choosing the value of confidence interval (α) [32]. The confidence interval (α) of 5% was used in the present work. This implies that 95% ($1 - \alpha$) of the confidence intervals would comprise the correct response. Accordingly, the influence of wear parameters (speed, normal load and time) on cumulative mass loss was determined. The normal load is obviously the main factor influencing the tribological properties of the three Al–Si alloy compositions. However, slightly different responses could be noticed form Figure 12 as function of composition. Both normal load and speed have significant impact on the mass loss of Al–1.3%Si and Al–1.5%Si alloys as illustrated in Figure 12a,b, respectively. The interaction of the three factors is minimum in Al–1.3%Si alloy as compared to other experimental conditions. On the other hand, Al–1.5%Si alloy is highly influenced by the interaction of the three factors as compared to that of Al–1.3%Si alloy. The situation differs somewhat in the effect of controlled factors on the mass loss of Al–13.5%Si, shown in Figure 12c. Although the normal load is the main influencing factor on the mass loss, the time has more effect than the speed and the interaction among the three factors is minimum.

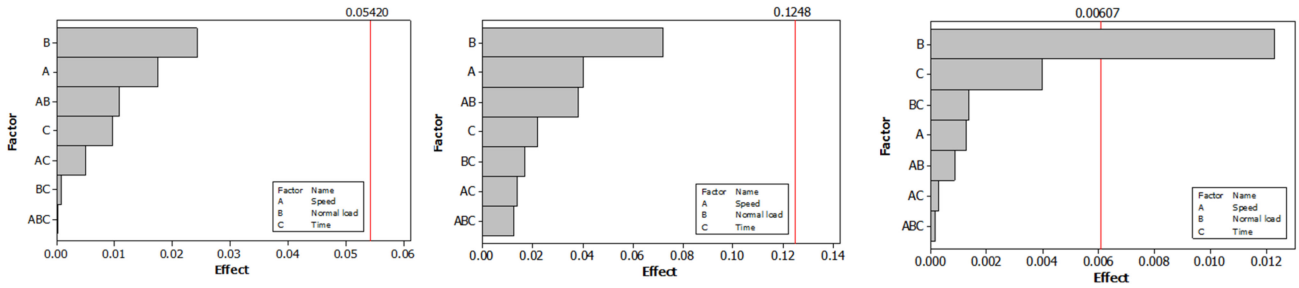

(**a**) (**b**) (**c**)

Figure 12. Pareto charts of the main effect of parametric interaction for (**a**) Al–1.3%Si, (**b**) Al–1.5%Si and (**c**) Al–13.5%Si alloys.

4. Conclusions

In this work, the microstructure, mechanical properties and wear behavior of Al–*x*%Si alloys (x = 1.3, 1.5, and 13.5) were examined and discussed. The specimens were prepared to examine the Al-rich terminal solid solution (using Al–1.3%Si alloy), hypoeutectic region (using Al–1.5%Si alloy), and hypereutectic region (using Al–13.5%Si alloy). The microstructures of the examined alloys showed a typical Al–Si eutectic structure in the three compositions with significant differences in their phase amounts and morphologies. The average microhardness number increased with the increase in Si concentration. The highest average microhardness number (47.16 HV) was acquired from the Al–13.5%Si alloy due to the presence of a significant amount of the hard phase (*Diamond Si*) compared with the other two compositions. However, when the soft phase (*FCC-Al*) dominated the structure, the average microhardness number dropped to 36.82 and 35.38 HV for the Al–1.5%Si and Al–1.3%Si alloys, respectively. The mechanical behavior analysis proved that the Al–1.3%Si alloy can be easily cold-worked because of the high strain hardening exponent value (0.3193), as compared to the hypoeutectic and hypereutectic samples. The cumulative mass loss increased when both the rotational speed and normal load were increased as a function of time. A direct relationship between the wear resistance and microhardness number was depicted from the experimental results. Furthermore, samples with a high microhardness number showed a lower surface roughness index value. The response surfaces of the mass loss vs. speed, normal load and time showed increased mass loss when the three controlled parameters were increased. However, Pareto charts of the main effects of parametric interactions showed that the normal load is the main factor that must be taken in consideration when studying the tribological properties of Al–Si alloys.

Author Contributions: Conceptualization, A.M.; Methodology, A.M. and N.A.; Software, A.M.; Validation, A.M. and N.A.; Formal analysis, A.M.; Investigation, A.M. and N.A.; Data curation, A.M. and N.A.; writing—original draft, A.M.; writing—review and editing, A.M. and N.A.; Visualization, A.M.; Supervision, A.M. and N.A.; Project administration, A.M. All authors have read and agreed to the published version of the manuscript.

Funding: This research received no external funding.

Institutional Review Board Statement: Not applicable.

Informed Consent Statement: Not applicable.

Data Availability Statement: Not applicable.

Acknowledgments: The authors thankfully acknowledge the support provided by the Tafila Technical University by granting access to all research facilities during the research period.

Conflicts of Interest: The authors declare no conflict of interest.

References

1. Ceschini, L.; Toschi, S. Friction and Wear of Aluminum Alloys and Composites. In *Friction, Lubrication, and Wear Technology*; ASM International: Materials Park, OH, USA, 2017; pp. 509–532.
2. Anand, S.; Srivatsan, T.S.; Wu, Y.; Lavernia, E.J. Processing, Microstructure and Fracture Behaviour of a Spray Atomized and Deposited Aluminium–Silicon Alloy. *J. Mater. Sci.* **1997**, *32*, 2835–2848. [CrossRef]
3. Goñi, J.V.; Rodriguez-Ibabe, J.M.; Urcola, J.J. Strength and Toughness of Semi-Solid Processed Hypereutectic AlSi Alloys. *Scr. Mater.* **1996**, *34*, 483–489. [CrossRef]
4. Prasada Rao, A.K.; Das, K.; Murty, B.S.; Chakraborty, M. Effect of Grain Refinement on Wear Properties of Al and Al–7Si Alloy. *Wear* **2004**, *257*, 148–153. [CrossRef]
5. Raju, K.; Harsha, A.P.; Ojha, S.N. Microstructural Features, Wear, and Corrosion Behaviour of Spray Cast Al–Si Alloys. *Proc. Inst. Mech. Eng. Part J J. Eng. Tribol.* **2011**, *225*, 151–160. [CrossRef]
6. Meena, P.C.; Sharma, A.; Singh, S. Effect of Grain Refinement on Microstructure and Wear Behavior of Cast Al–7Si Alloys. *Metall. Ital.* **2015**, *107*, 25–34.
7. Barrirero, J. *Eutectic Modification of Al–Si Casting Alloys*; Linköping Studies in Science and Technology Dissertations No. 2014; Linköping University Electronic Press: Linköping, Sweden, 2019; Volume 2014, ISBN 9789175190075.
8. Kaufman, J.G.; Rooy, E.L. *Aluminum Alloy Castings: Properties, Processes, and Applications*; Benedyk, J.C., Ed.; ASM International: Materials Park, OH, USA, 2004; ISBN 978-0-87170-803-8.
9. Panemangalore, D.B.; Shabadi, R. Microstructural Aspects of Metal-Matrix Composites. In *Encyclopedia of Materials: Composites*; Elsevier: Amsterdam, The Netherlands, 2021; pp. 274–297.
10. Karl-Heinz, Z.G. (Ed.) Microstructure and Wear of Materials. In *Tribology Series*; Elsevier: Amsterdam, The Netherlands, 1987; pp. 351–495, ISBN 9780444427540.
11. Yasmin, T.; Khalid, A.A.; Haque, M.M. Tribological (Wear) Properties of Aluminum–Silicon Eutectic Base Alloy under Dry Sliding Condition. *J. Mater. Process. Technol.* **2004**, *153–154*, 833–838. [CrossRef]
12. Dwivedi, D.K. Wear Behaviour of Cast Hypereutectic Aluminium Silicon Alloys. *Mater. Des.* **2006**, *27*, 610–616. [CrossRef]
13. Kori, S.A.; Chandrashekharaiah, T.M. Studies on the Dry Sliding Wear Behaviour of Hypoeutectic and Eutectic Al–Si Alloys. *Wear* **2007**, *263*, 745–755. [CrossRef]
14. Alshmri, F.; Atkinson, H.V.; Hainsworth, S.V.; Haidon, C.; Lawes, S.D.A. Dry Sliding Wear of Aluminium-High Silicon Hypereutectic Alloys. *Wear* **2014**, *313*, 106–116. [CrossRef]
15. Mostafa, A.; Medraj, M. Binary Phase Diagrams and Thermodynamic Properties of Silicon and Essential Doping Elements (Al, As, B, Bi, Ga, In, N, P, Sb and Tl). *Materials* **2017**, *10*, 676. [CrossRef]
16. *SGTE Substance Database*; Royal Institute of Technology: Stockholm, Sweden, 1994.
17. Bale, C.W.; Bélisle, E.; Chartrand, P.; Decterov, S.A.; Eriksson, G.; Gheribi, A.E.; Hack, K.; Jung, I.-H.; Kang, Y.-B.; Melançon, J.; et al. FactSage Thermochemical Software and Databases, 2010–2016. *Calphad* **2016**, *54*, 35–53. [CrossRef]
18. *ASTM G99 Standard*; Test Method for Wear Testing with a Pin-on-Disk Apparatus. ASTM International: West Conshohocken, PA, USA, 2016.
19. Zaid, A.I.O.; Mostafa, A.O. Effect of Hafnium Addition on Wear Resistance of Zinc–Aluminum 5 Alloy: A Three-Dimensional Presentation. *Adv. Mater. Lett.* **2017**, *8*, 910–915. [CrossRef]
20. Ghassemi, M.H.; Abouei, V.; Moshtaghi, M.; Noghani, M.T. The Effect of Removing Worn Particles by Ultrasonic Cleaning on the Wear Characterization of LM13 Alloy. *Surf. Eng. Appl. Electrochem.* **2015**, *51*, 382–388. [CrossRef]
21. Gupta, M.; Ling, S. Microstructure and Mechanical Properties of Hypo/Hyper-Eutectic Al–Si Alloys Synthesized Using a near-Net Shape Forming Technique. *J. Alloys Compd.* **1999**, *287*, 284–294. [CrossRef]
22. Uguz, A.; Bayram, A. Effect of Si Content and Microstructure on the Wear Behaviour of Al-Si Alloys. *Metall* **2001**, *55*, 516–519.
23. Mostafa, A.O. Mechanical Properties and Wear Behavior of Aluminum Grain Refined by Ti and Ti + B. *Int. J. Surf. Eng. Interdiscip. Mater. Sci.* **2019**, *7*, 1–19. [CrossRef]
24. Barrirero, J.; Pauly, C.; Engstler, M.; Ghanbaja, J.; Ghafoor, N.; Li, J.; Schumacher, P.; Odén, M.; Mücklich, F. Eutectic Modification by Ternary Compound Cluster Formation in Al–Si Alloys. *Sci. Rep.* **2019**, *9*, 5506. [CrossRef]
25. Samuel, A.M.; Elgallad, E.M.; Doty, H.W.; Valtierra, S.; Samuel, F.H. Effect of Metallurgical Parameters on the Microstructure, Hardness Impact Properties, and Fractography of Al–(6.5–11.5) wt% Si Based Alloys. *Mater. Des.* **2016**, *107*, 426–439. [CrossRef]
26. Matusevich, A.E.; Massa, J.C.; Mancini, R.A. Computation of Tensile Strain-Hardening Exponents through the Power-Law Relationship. *J. Test. Eval.* **2012**, *40*, 104226. [CrossRef]
27. Silva, R.; Pinto, A.; Kuznetsov, A.; Bott, I. Precipitation and Grain Size Effects on the Tensile Strain-Hardening Exponents of an API X80 Steel Pipe after High-Frequency Hot-Induction Bending. *Metals* **2018**, *8*, 168. [CrossRef]
28. Odabas, D. Effects of Load and Speed on Wear Rate of Abrasive Wear for 2014 Al Alloy. *IOP Conf. Ser. Mater. Sci. Eng.* **2018**, *295*, 012008. [CrossRef]
29. Ozioko, F.U. Synthesis and Study on Effect of Parameters on Dry Sliding Wear Characteristics of Al–SI Alloys. In *Leonardo Electronic Journal of Practices and Technologies*; Technical University of Cluj-Napoca: Cluj-Napoca, Romania, 2012; pp. 39–48.

30. Arnell, D. Mechanisms and Laws of Friction and Wear. In *Tribology and Dynamics of Engine and Powertrain*; Elsevier: Amsterdam, The Netherlands, 2010; pp. 41–72.
31. Baby, A.K.; Priyaranjan, M.; Deepak Lawrence, K.; Rajendrakumar, P. Tribological Behaviour of Hypereutectic Al–Si Automotive Cylinder Liner Material under Dry Sliding Wear Condition in Severe Wear Regime. *Proc. Inst. Mech. Eng. Part J J. Eng. Tribol.* **2021**, *235*, 1450–1462. [CrossRef]
32. Maawad, E.; Brokmeier, H.-G.; Wagner, L.; Sano, Y.; Genzel, C. Investigation on the Surface and Near-Surface Characteristics of Ti–2.5Cu after Various Mechanical Surface Treatments. *Surf. Coat. Technol.* **2011**, *205*, 3644–3650. [CrossRef]